Quantitative comparison of thermal dose models in normal canine brain

Joshua P. Yung
Department of Imaging Physics, The University of Texas M. D. Anderson Cancer Center,
1515 Holcombe Boulevard, Houston, Texas 77030 and The University of Texas Graduate School of
Biomedical Sciences at Houston, 6767 Bertner Avenue, Houston, Texas 77030

Anil Shetty and Andrew Elliott
Department of Imaging Physics, The University of Texas M. D. Anderson Cancer Center,
1515 Holcombe Boulevard, Houston, Texas 77030

Jeffrey S. Weinberg
Department of Neurosurgery, The University of Texas M. D. Anderson Cancer Center,
1515 Holcombe Boulevard, Houston, Texas 77030

Roger J. McNichols and Ashok Gowda
BioTex, Inc., 8058 El Rio Drive, Houston, Texas 77054

John D. Hazle and R. Jason Stafford[a]
Department of Imaging Physics, The University of Texas M. D. Anderson Cancer Center,
1515 Holcombe Boulevard, Houston, Texas 77030 and The University of Texas Graduate School of
Biomedical Sciences at Houston, 6767 Bertner Avenue, Houston, Texas 77030

Purpose: Minimally invasive thermal ablative therapies as alternatives to conventional surgical management of solid tumors and other pathologies is increasing owing to the potential benefits of performing these procedures in an outpatient setting with reduced complications and comorbidity. Magnetic resonance temperature imaging (MRTI) measurement allows existing thermal dose models to use the spatiotemporal temperature history to estimate the thermal damage to tissue. However, the various thermal dose models presented in the literature employ different parameters and thresholds, affecting the reliability of thermal dosimetry. In this study, the authors quantitatively compared three thermal dose models (Arrhenius rate process, CEM_{43}, and threshold temperature) using the dice similarity coefficient (DSC).
Methods: The DSC was used to compare the spatial overlap between the region of thermal damage as predicted by the models for *in vivo* normal canine brain during thermal therapy to the region of thermal damage as revealed by contrast-enhanced T1-weighted images acquired immediately after therapy (<20 min). The outer edge of the hyperintense rim of the ablation region was used as the surrogate marker for the limits of thermal coagulation. The DSC was also used to investigate the impact of varying the thresholds on each models' ability to predict the zone of thermal necrosis.
Results: At previously reported thresholds, the authors found that all three models showed good agreement (defined as $DSC > 0.7$) with post-treatment imaging. All three models examined across the range of commonly applied thresholds consistently showed highly accurate spatial overlap, low variability, and little dependence on temperature uncertainty. DSC values corresponding to cited thresholds were not significantly different from peak DSC values.
Conclusions: Thus, the authors conclude that the all three thermal dose models can be used as a reliable surrogate for postcontrast tissue damage verification imaging in rapid ablation procedures and can also be used to enhance the capability of MRTI to control thermal therapy in real time. © *2010 American Association of Physicists in Medicine.* [DOI: 10.1118/1.3490085]

Key words: laser-induced thermal therapy, magnetic resonance imaging-guided thermal therapy, magnetic resonance thermal imaging, thermal dosimetry, brain

I. INTRODUCTION

Minimally invasive thermal ablative therapy as an alternative to conventional surgery in the treatment of solid tumors and other pathologies is increasing in use because of the potential benefits of performing these procedures in an outpatient setting with reduced complications and comorbidity. Using real-time magnetic resonance (MR) imaging to guide these minimally invasive ablative procedures is desirable because of the multiple contrast mechanisms currently available for treatment planning, targeting, monitoring, and verification. In particular, the use of MR temperature imaging (MRTI) to monitor energy delivery in real time has facilitated a safer and more effective therapy delivery for modalities and tumor locations which previously would have been too difficult to attempt.[1,2]

Recently, a FDA-cleared MR-guided laser-induced ther-

mal therapy was used to treat intracerebral lesions in a clinical trial.[2] This system uses MRTI based on the proton resonance frequency shift to guide the delivery of therapy in real time with a temperature uncertainty generally less than 2 °C.[3,4] The cumulative spatiotemporal temperature history is then used to estimate the thermal damage to tissue.[5,6] This modeling of thermal damage can potentially be used as a surrogate for post-treatment damage verification imaging and can also be used to control therapy delivery in real time.

Studies have shown that precontrast and postcontrast imaging of brain ablations/thermal lesions in the brain reveals regions of thermal necrosis correlating with those identified by post-treatment histopathologic analysis.[7,8] However, contrast-enhanced imaging is not amenable to real-time procedure monitoring as irreversible damage may have already occurred. Multiple contrast injections would also require time for washout prior to each injection and risk toxicity issues. With accurate MR thermometry and thermal dose prediction, one should be able to monitor treatments in real time and terminate them immediately before any adjoining healthy tissue was damaged. This ability would enhance the safety and efficiency of these minimally invasive thermal ablative procedures. Additionally, accurate dosimetry, when coupled with accurate simulation of heating during treatment, would enable better prospective planning of thermal ablative procedures.

Various models of tissue damage have been evaluated in brain tissue for rapid thermal therapy delivery applications, such as laser or focused-ultrasound technology.[5,9,10] The irreversible denaturation of proteins is assumed to be the rate-limiting step in heating-induced tissue coagulation and also has been shown to be directly correlated with cell death.[11–13] Tissue damage can be modeled as a change in state based on an Arrhenius rate process.[14,15] Henriques[15] successfully used the Arrhenius model to predict coagulation in human and pig skin; more recently, this model has been applied to brain tissue.[9,16,17] Sapareto and Dewey[16] developed the CEM_{43} model as a simplification of the Arrhenius model via approximation and normalization to hyperthermia results and used it to predict the isoeffects that would be produced if the tissue had been exposed to a cumulative equivalent number of minutes at 43 °C (CEM_{43}). The CEM_{43} model was then later extended to high-temperature ablations by Damianou *et al.*[18] Lastly, the simplest thermal dose model to apply is a simple temperature threshold, which assumes that tissue is damaged nearly instantaneously once it reaches a certain temperature.[19] This model is different from the others in that it assumes that the tissue response is independent of the temperature history, which may be a reasonable approximation in cases of rapid ablation.

Although these models have all been used to predict damage in brain tissue during thermal ablative treatment, even within the same model, widely varying parameters or thresholds have been used as an indication of thermal damage defined by their respective end points. For instance, studies using the CEM_{43} model to predict damage to brain tissue resulted in different values including 28 min, with a standard

deviation of 41 min (Ref. 20) over seven lesions, when compared to post-treatment T2-weighted imaging 4 h after therapy and 50 min (Ref. 8) has been used for comparison to post-treatment contrast-enhanced T1-weighted imaging 20 min after therapy. Likewise, in studies using the Arrhenius model, different parameters and thresholds have been used to predict cell death: Thermal damage threshold, $\Omega = 1$,[9,16] and $\Omega = 6.9$.[10] Temperature thresholds have been reported in the range of 48 to 53 °C.[5,20,21]

In this work, we evaluated how accurately the three thermal dose models (Arrhenius rate process, CEM_{43}, and threshold temperature) could function as a surrogate to contrast-enhanced (i.e., "perfusion weighted") imaging of the region of damage of normal canine brain tissue after laser ablative therapy by comparing the predictions to postcontrast T1-weighted images acquired immediately after treatment (<20 min). To quantitatively evaluate the performance of each thermal dose model, we used a statistical validation metric, the dice similarity coefficient (DSC), to measure the spatial overlap of regions.[22] The DSC has previously been used to measure image segmentation accuracy in brain tissue with MR images.[23–25] Post-treatment contrast-enhanced T1-weighted imaging was used as the gold standard in order to validate the use of MR-derived thermal dosimetry as a surrogate for postcontrast thermal damage verification imaging of brain tissue. After the administration of a contrast agent, the peripheral region of enhancement surrounding the nonperfused zone has been shown to be in good agreement with histologic findings as a marker for thermal coagulation.[8,26,27] One such study by Breen *et al.*[7] showed that the tissue within the hyperintense and central regions closely corresponded to the region of dead or irreversibly damaged cells in histology. Their experiment consisted of carefully acquiring MR and tissue images in the same plane, which were later aligned for comparison and cell-viability staining techniques.

In this study, we used the DSC to quantitatively compare the spatial overlap of the region of thermal damage as predicted by the Arrhenius, CEM_{43}, and temperature threshold models for *in vivo* normal canine brain during thermal therapy to the region of thermal damage, as revealed by contrast-enhanced T1-weighted images acquired immediately after therapy (<20 min). We also used the DSC to investigate the effect that varying the parameters and thresholds had on each model.

II. MATERIALS AND METHODS

II.A. MR-guided laser-induced thermal therapy

All experimental procedures were performed at The University of Texas M. D. Anderson Cancer Center in accordance with protocols approved by the Institutional Animal Care and Use Committee. Four clinically normal mongrel hound dogs (weighing 20–25 kg each) were used. To image and treat the dogs, we induced anesthesia with intramuscular medetomidine (10 mg/kg) and maintained it with 2% isoflurane. Before laser treatment, a burr hole was created in the right parietal bone of each anesthetized dog. Briefly, a 1 cm

light-diffusing tip fiber encased in an actively cooled sheath was inserted into the frontal lobe. Laser fiber placement was planned and verified by using a 3D fast, spoiled gradient-echo imaging sequence. All imaging was performed on a 1.5 T whole-body MR scanner (Excite HD, GE Healthcare, Waukesha, WI), with an eight-channel phased array, receive-only head coil (MRI Devices Corp., Gainesville, FL). Using a temperature-sensitive echo-planar sequence combined with parallel imaging, we obtained real-time monitoring of the temperature changes during exposure of normal brain tissue to the laser (980 nm; 6–10 W) in five planes every 6 s (number of shots=8; echo time (TE)=20 ms; repetition time (TR)=544 ms; field of view (FOV)=20 cm×20 cm; frequency×phase=256×128; bandwidth (BW) =±250 kHz).[28,29] A water-selective spatial-spectral excitation was used in order to minimize errors due to the lipid signal contamination. Coil sensitivities from a calibration scan were combined to produce the phase maps. Voxel dimensions were 0.78 mm×0.78 mm with a slice thickness of 3–4 mm. Three to five planes were acquired parallel to one another and acquired parallel to the laser fiber with the center plane positioned overlapping the fiber. The acceleration factor was 1–2 for all subjects. Subsequent post-treatment MR imaging consisted of postcontrast T1-weighted fast-spin echo imaging (TE=9.2 ms; TR=800 ms; FOV=20 cm×20 cm; frequency×phase=256×192; BW=±25 kHz) with no acceleration factor applied. The spatial resolution and slice location of the post-treatment imaging matched the MR temperature images. After therapy, the burr hole was sealed with bone wax, the muscle was closed with 3.0 vicryl sutures, and the skin was closed with 3.0 nylon sutures.

II.B. Postprocessing of real-time MRTI and thermal dose

MRTI was performed using the temperature-dependent proton resonance frequency method.[3] An in-house software written in MATLAB (The Mathworks Inc., Natick, MA) was used to process the temperature images and to apply the thermal dose models. Temperature changes were calculated from complex phase subtraction images and added to the baseline temperature of the dogs to obtain absolute temperature maps. The relationship between the phase difference ($\Delta\varphi$) and the measured temperature change (ΔT) can be expressed as

$$\Delta T = \frac{\Delta\varphi}{2\pi \cdot \alpha \cdot \gamma B_0 \cdot TE}, \tag{1}$$

where α is the temperature sensitivity coefficient (assumed to be -0.0097 ppm/$^\circ$C),[30] γ is the gyromagnetic ratio (42.58×10^6 Hz/T), B_0 is the strength of the main magnet (1.5 T), and TE is the echo time for the MR pulse sequence (20 ms).

By defining a region of interest (ROI) in the first three temperature images before treatment delivery, we were able to estimate the uncertainty (noise) in the temperature images as the average of the standard deviations from the ROI. The ROI was placed as close as possible to the active area of the
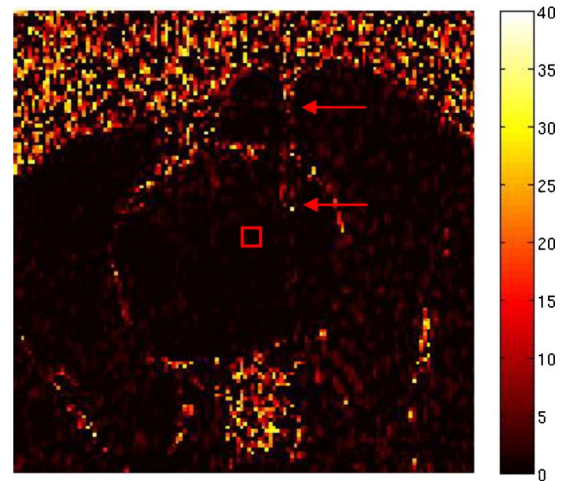

FIG. 1. Map of the temperature rise in °C obtained prior to heating showing the ROI (square) used to determine temperature uncertainty in the MRTI. The laser fiber (arrows) was avoided to prevent the water-cooled sheath from affecting the temperature measurement.

laser fiber in order to measure the uncertainty of the ablation region. Figure 1 shows the ROI for dog 1. The area to the right of the ROI, where temperature artifacts due to the laser fiber can be observed, was avoided to prevent the water-cooled sheath from affecting the temperature measurement.

Magnetic field drift was accounted for by creating an additional ROI in the contralateral side of the brain away from the area of heating and the mean temperature at each time point was subtracted from its respective time point's temperature measurements.

Post-treatment MR images were registered to the same anatomical location as the images acquired during MRTI; they were then manually segmented at the same slice location as the center plane of the MRTI. The outer edge of the hyperintense rim of the ablation region was used as the surrogate marker of the isoeffect for thermal coagulation. Manual segmentation was performed in MATLAB without prior knowledge of the estimated dose and included the signal void left by the laser applicator. The window and level settings for each MR image were modified to provide sufficient contrast between the hyperintense rim and the adjacent tissue without increasing the identifiable lesion size or shape. Voxels along and within the segmentation border were given a value of 1 and assumed to be damaged beyond repair, while voxels outside of the segmentation border were given a value of 0 and considered to be viable. Several segmentations were performed for each dog in order to accommodate the variance in this procedure. The average measurement was used for comparison with the MRTI-derived dosimetry.

Important preprocessing and postprocessing steps for the temperature maps that improved comparison with the post-treatment images included eliminating temperature images obtained prior to heating, filtering, correcting empty pixels in the damage estimate interior, and obtaining accurate image registration. In one dog, a wiener filter was applied to the post-treatment images prior to segmentation. The first image

of the echo-planar sequence was skipped as a reference image for the complex phase subtraction as the signal had not reached steady state yet.

Absolute temperature maps were input into the thermal dose models to obtain a predicted region of damage. Each model was applied on a pixel-by-pixel basis. Voxels that reached the threshold for thermal damage or thermal dose were assumed to be damaged beyond repair. The temporal temperature histories at each pixel were used in the Arrhenius rate process model[14]

$$\Omega(t) = \int_0^t A e^{-E_A/RT(\tau)} d\tau. \tag{2}$$

In this model, the frequency factor A and the activation energy E_A are kinetic parameters experimentally determined *a priori*. In this study, the values for A and E_A were 3.1×10^{98}/s and 6.28×10^5 J/mol, respectively. These values are the same as those derived by Henriques from his experimental data with the basal epidermis layer and have been used in previous studies.[2,9,10,16] $T(\tau)$ is the tissue temperature over time and R is the universal gas constant. The threshold $\Omega(t)$ was varied from 0.01 to 10.2 with Ω equal to 1.0 being used as the norm from previous reports.[2,9] The CEM_{43} model, which is based on the Arrhenius model, quantifies the damage in a nonlinear fashion using the temporal temperature history and relates it to a constant temperature of 43 °C (Ref. 31)

$$CEM_{43} = \sum_{t=0}^{t=\text{final}} R^{43-\bar{T}} \Delta t, \tag{3}$$

where CEM_{43} is the cumulative equivalent time at the reference temperature of 43 °C, T is the average temperature during period Δt, and R is a constant. At temperatures at or above 43 °C, R was set equal to 0.5; at temperatures below 43 °C, R was set equal to 0.25, which agrees with previous implementations.[32] For this model, Sapareto and Dewey[31] chose a break temperature of 43 °C as the best estimate from the available data. The thermal dose at which tissue was considered to be dead was varied from 10 CEM_{43} to 1200 CEM_{43}. In the present study, 240 CEM_{43} was taken to be the norm, based on previous studies.[33–35] In this model, disregarding the temperature history of the subject, lethal thermal damage was assumed to occur above a critical temperature, with nonlethal thermal damage occurring below the threshold temperature. We varied the threshold temperature from 51 to 71 °C; 57 °C is the threshold temperature reported in previous studies.[36]

II.C. Quantitative comparison of dose models

To quantitatively compare the region of damage predicted by each model as a function of threshold value, we used the DSC to calculate the spatial overlap between the binary images of the model output and the manually segmented posttreatment images. The DSC has been recommended as a good validation metric for spatial overlap.[37] The DSC is defined as
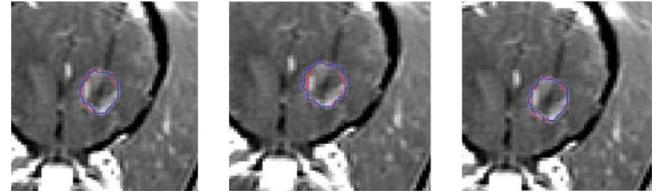

FIG. 2. Damage revealed on the postcontrast T1-weighted image and the damage estimates produced by the models in dog 4 (left, Arrhenius; middle, CEM_{43}; right, temperature threshold). The outline of the damage estimate is overlaid onto the outline of the thermally damaged region identified by the postcontrast image.

$$DSC(A,B) = 2(A \cap B)/(A + B). \tag{4}$$

The possible values of DSC range from 0 (no overlap) to 1 (complete overlap). For the purposes of this study, a DSC value greater than 0.7 was assumed to be a "good" agreement.[23]

III. RESULTS

III.A. MR-guided laser-induced thermal therapy

According to the MRTI feedback on the MR-guided laser-induced thermal therapy system, the intracranial laser treatment created elliptical lesions between 1.5 and 2 cm along the fiber and 1.0–1.5 cm transverse to the fiber. Applied powers were manually modulated and varied from 6 to 15 W, with pulses lasting between 19 and 189 s. The water-cooled sheath prevented tissue charring adjacent to the laser fiber.

III.B. Postprocessing of real-time MRTI and thermal dose

We examined the slice locations of the post-treatment images that were closest to the center plane of the MRTI. Manual segmentation was performed on the postcontrast T1-weighted images acquired immediately following the treatment (<20 min). Using the laser fiber as an internal marker, the post-treatment images were well registered with the images acquired during treatment. The damaged tissue and hyperintense rim were measured from the postcontrast T1-weighted images. The areas of the damaged regions for the four dogs were 75.07, 117.18, 140.99, and 99.08 mm².

III.C. Comparison of dose models

Using the DSC to quantitatively evaluate the change in spatial overlap, we implemented various thresholds. Figure 2 shows the estimates of tissue damage generated by each model overlaid onto the postcontrast T1-weighted image for dog 4. There was good agreement between the thermally damaged region identified by the different damage models and the thermally damaged region as identified by the postcontrast image and similar results were obtained for all other dogs.

For the Arrhenius model, the standard threshold of $\Omega = 1$ gave DSC values of 0.92, 0.88, 0.92, and 0.92 for the four dogs, with a mean DSC ± standard deviation of 0.91 ± 0.02. The maximum DSC (DSC = 0.91 ± 0.03) obtained averaging
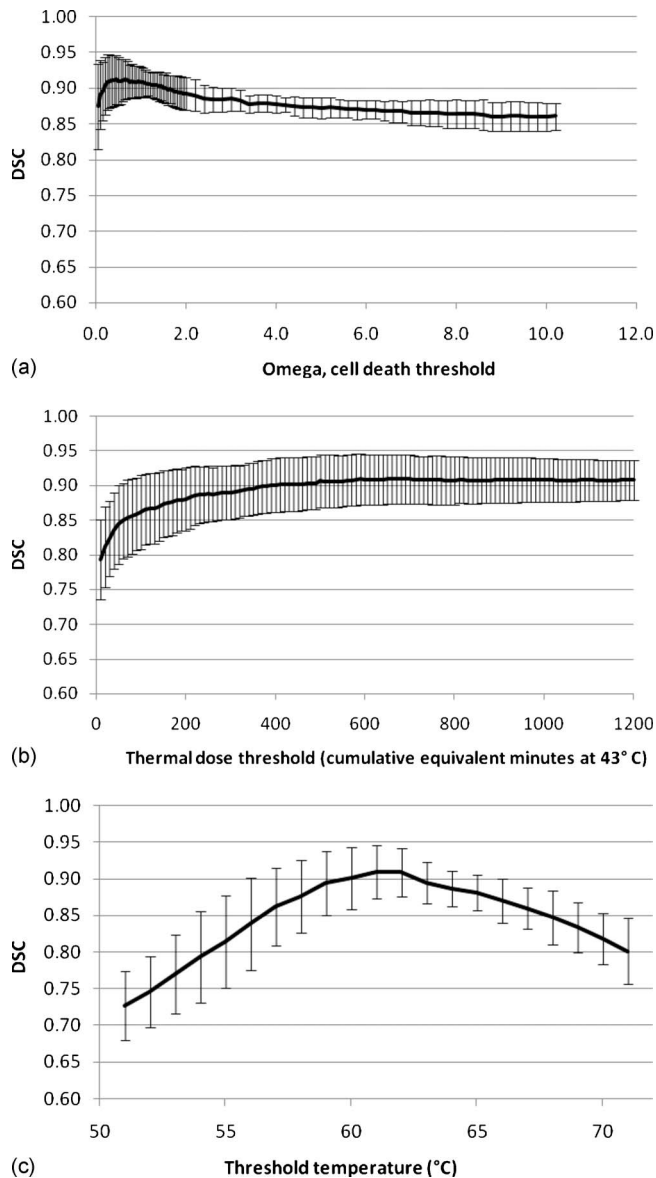
FIG. 3. DSC values averaged from the four dogs using the (a) Arrhenius, (b) CEM$_{43}$, and (c) threshold temperature models. Error bars represent the standard deviation of each threshold that was examined. A temperature uncertainty was added and subtracted from the measured baseline temperature and the resulting DSC values were consistently within the standard deviation.

over the four subjects occurred at $\Omega = 0.65$ (Fig. 3). For the CEM$_{43}$ model, at the assumed threshold of 240 CEM$_{43}$, DSC values for the four dogs were 0.87, 0.84, 0.92, and 0.91, with a mean of 0.89 ± 0.04. The DSC value reached a maximum (DSC$=0.91 \pm 0.04$) for the threshold tested at a thermal threshold of 690 CEM$_{43}$ averaged over the four dogs. For the temperature threshold model, a threshold of 57 °C resulted in DSC values of 0.86, 0.79, 0.91, and 0.88 for the four dogs and a mean of 0.86 ± 0.05. The maximum DSC (DSC $=0.91 \pm 0.04$) averaged over the four dogs occurred at a threshold temperature of 61 °C. The threshold intervals that resulted in DSC values within one standard deviation of maximum DSC acquired in this study were 0.10–3.0,

≥ 160 min, and 58–65 °C for the Arrhenius, CEM$_{43}$, and temperature threshold models, respectively. DSC values corresponding to cited thresholds were not significantly different from maximum DSCs for all three models.

Previously cited thresholds resulted in DSC values ranging from 0.88 to 0.92, 0.84 to 0.92, and 0.79 to 0.91 for the Arrhenius, CEM$_{43}$, and temperature threshold models, respectively. For all models applied to all of the dogs, the DSC values were well over 0.7, the threshold commonly thought to correspond to a "good" spatial overlap between images.[23] At least 90% spatial overlap was obtained for all four dogs when using thresholds of $\Omega = 0.2$–1.45, CEM$_{43} \geq 390$ min, and T$=60$ °C–62 °C, for the Arrhenius, CEM$_{43}$, and temperature threshold model, respectively. The upper bound of the range for the CEM$_{43}$ model was beyond the thresholds tested in this study. Table I summarizes the thresholds for each model and corresponding DSC values.

The average of the ROI standard deviations from the first three temperature maps prior to treatment delivery resulted in different temperature uncertainties for each dog. The uncertainty of the temperature measurements for the four dogs were 0.32, 0.76, 0.47, and 0.31 °C, which, when added and subtracted from the dogs' measured baseline temperature, resulted in new baselines (Table II) that were used to convert the relative temperature maps to new absolute temperature maps. Each new temperature map for each dog allowed for an additional DSC plot to be generated. Tables III and IV summarize the thresholds for each model and corresponding DSC values after applying these temperature uncertainties to the temperature maps. All three models at their respective peaks in DSC values had little dependence on the small variations within the temperature maps. The Arrhenius and CEM$_{43}$ models showed a large range in thresholds that resulted in a spatial overlap which was not statistically different from the maximum DSC values found in the range of thresholds tested. With the inclusion of the temperature uncertainties, the Arrhenius and threshold temperature models' DSC values greater than 0.9 converged on a range of threshold values that continued to include values previously reported in the literature.

IV. DISCUSSION

In this study, the previously reported parameters for each model ($\Omega = 1$, CEM$_{43} = 240$ min, and T$=57$ °C) resulted in high DSC values when compared to the thermal tissue damage as identified by the contrast-enhanced images acquired immediately post therapy. This corresponded to a high degree of accuracy in the damage predictions for rapid ablation procedures. Utilization of parameters different from these previously cited thresholds did not result in statistically different DSC values. It is important to note that the impact of threshold values investigated is relevant to the experimental parameters used in this study. Differences in the experimental setup and measurement methodology may produce alternative thresholds.

Thresholds near peak DSC values had little dependence on temperature uncertainty. The use of a cooled-catheter 980

TABLE I. Threshold and DSC values for cited and maximum DSC threshold values with threshold intervals within 1σ of DSC_{max} and for all four dogs to have $DSC \geq 0.9$.

	Thresholds			
Model	Cited	DSC_{max}	$DSC_{max} + 1\sigma$	$DSC \geq 0.9$
Arrhenius (Ω)	$\Omega = 1.0$	$\Omega = 0.65$	0.10–3.0	0.2–1.45
DSC	0.91 ± 0.02	0.91 ± 0.03		
CEM_{43} (min)	240	690	≥ 160	≥ 390
DSC	0.89 ± 0.04	0.91 ± 0.04		
Threshold temperature (°C)	57	61	58–65	60–62
DSC	0.86 ± 0.05	0.91 ± 0.04		

nm laser running at higher powers in this study may have caused the temperature gradient near the edge of the lesion to be sharper than previous investigations using slower heating with Nd:YAG or 810 nm lasers.[20,27] The sensitivity of the thermal damage model on the chosen threshold is likely to be reduced due to the sharper temperature gradients across the narrow spatial boundary between damaged and undamaged tissue, which would allow for a larger range of thresholds to still accurately predict the damage.

The simple threshold temperature model, which, unlike the other two models does not account for the temperature history during treatment, also predicted areas of damage agreeing with postcontrast images with a fair degree of accuracy. The short duration and high temperature of the treatment may have diminished the importance of the temperature history.

For the CEM_{43} model, DSC values slightly increased for the higher thresholds applied in this study, which were higher than thresholds used in other published studies. This can be explained in part by the steep spatial gradients for damage that would cause large thermal dose values from the exponential behavior of the model while making minimal difference to our spatial overlap metric.[20,21,38] Besides obtaining an accurate prediction of the damaged region, this model also had repeatability and small deviations among the subjects. One difference in our experimental process compared to other studies which may have helped was that we performed post-treatment imaging immediately after therapy (<20 min). Other studies, such as in Chen *et al.*,[20] acquired post-treatment imaging 4 h after therapy. The shorter time period may have prevented tissue swelling effects from being introduced into our analysis; the effects of swelling may account for the lower damage thresholds in the study by Chen *et al.* and other previous studies. In longitudinal studies performed by Kangasniemi *et al.*,[8] the lesion was periodically

TABLE II. Measured baseline temperatures and temperature uncertainties.

Dog	Baseline ± uncertainty
1	$34.3° \pm 0.32$
2	$35.9° \pm 0.76$
3	$33.9° \pm 0.47$
4	$34.3° \pm 0.31$

measured and shown to increase in size for several days after treatment and to return to its original size within 14 days; the 14-day size was also shown to correlate well with that measured from post-treatment imaging obtained immediately after therapy. Other studies have also reported the occurrence of post-treatment acute inflammation and edema followed by decrease in lesion size.[2,26,39,40] The difference in spatial resolution, registration, laser power, and heating duration may also have contributed to the discrepancy in results compared to previously published studies.

In this study, thresholds were applied to the Arrhenius model as a predictive model for thermal damage. Unlike other studies which use the Arrhenius model to describe the probability for cell death or protein coagulation as a function of temperature, in this study, the model was used to predict a specific end point. Differences in measurement methodology or experimental end point, such as the outer edge of the hypointense zone, will certainly produce a variation in threshold. The damage end point used in this study has been reported or used in other published reports.[7,8,26,27]

In this study, we used the DSC to quantitatively measure the spatial overlap between model-predicted damage and that evident on post-treatment images because of this technique's advantages over other methods. Receiver operating characteristic curves, another well-known validation metric, were not used because the chosen total area analyzed (which is arbitrary) would affect the curve's outcome.[41] A large area would have a large number of true negatives, which would boost specificity. A small area, such as the lesion area from post-treatment imaging, would prevent false positives from an overestimated damage prediction to be included in the metric. A correlation coefficient such as Bland–Altman[42] would be able to compare areas between the predicted lesion region and the post-treatment image, but would not include the spatial conformation (shape or contour) of the damaged region. Conversely, the DSC was calculated using only the damaged area and thus was not dependent on a user-determined area.

Note that a variety of laser powers and durations were applied in this study. For dogs 1 and 4, the lesions were created by a single pulse at 9 W for 189 s and 12 W for 50 s, respectively. For dogs 2 and 3, the lesions were created by multiple pulses with increasing power, ranging from 6 to

TABLE III. Threshold and DSC values for cited and maximum DSC threshold values with threshold intervals within 1σ of DSC_{max} and for all four dogs to have $DSC \geq 0.9$ after subtracting the temperature uncertainty from the baseline temperature.

Model	Thresholds			
	Cited	DSC_{max}	$DSC_{max} \pm 1\sigma$	$DSC \geq 0.9$
Arrhenius (Ω)	$\Omega = 1.0$	$\Omega = 0.55$	0.10–1.8	0.15–1.15
DSC	0.90 ± 0.02	0.91 ± 0.02		
CEM_{43} (min)	240	1160	≥ 200	≥ 310
DSC	0.89 ± 0.04	0.91 ± 0.02		
Threshold temperature (°C)	57	61	58–65	60–62
DSC	0.87 ± 0.05	0.91 ± 0.03		

13.2 W and 5.25 to 14.6W. The mixture of laser application did not result in a single lesion being more accurately predicted than the other lesions.

Limitations of this study consist of the small sample size (N=4) used as per recommendation by an in-house biostatician. A larger quantity of subjects would provide better statistics. The PRF temperature sensitivity coefficient has also been shown to vary due to the temperature-induced changes in the volume magnetic susceptibility and be dependent on the orientation and geometry of the heat-delivery device and heat pattern.[43] In this study, although post-treatment images were acquired immediately following thermal therapy, it is unknown whether the onset of tissue swelling had already begun.

The effect of temperature uncertainty on thermal dose models is a complicated one. An overestimation of thermal dose can be caused by the thermal noise in the models. For example, in the CEM_{43} model, a reduction by a factor of $e^{0.5\sigma^2 \ln^2 2}$ may be necessary in the presence of a normal distributed temperature noise with uncertainty σ due to the lognormal distribution of the dose. This reduction can be used to obtain zero error on average due to the temperature uncertainty. For the Arrhenius thermal dose function, the overestimation is not as simple due to inverse temperature dependence. With Taylor series expansion to approximate a lognormal distribution, the Arrhenius thermal dose model is simplified and an approximate reduction by $e^{0.5(E/RT_0^2)^2 \sigma^2}$, where T_0 is approximated to be the body temperature, is

needed to perform the same correction as in the CEM_{43} model's case. These factors will be investigated in more depth and included in future studies.

Although this study was performed on normal canine brain tissue, similar results would be expected in intracerebral tumors based on previously published works.[2,16] In this study, only canine brain tissue was studied; however, the use of MR-guided laser-induced thermal therapy has been examined in several other tissue types, including liver and prostate tissue. It is important to realize that a different set of parameters or thresholds may provide a better prediction for another type of tissue, given that studies have shown tissue damage due to thermal ablation can be tissue-type dependent.[5]

V. CONCLUSIONS

In summary, all three thermal dose models show excellent spatial overlap with the predicted thermal damage as measured by immediate post-treatment imaging (<20 min) for rapid ablation procedures. We found that for both the CEM_{43} and Arrhenius models, a wide range of thresholds resulted not only in highly accurate spatial overlap with post-treatment imaging but also in low variability. The threshold temperature model also had highly accurate spatial overlap and low variability but in a small range of threshold temperatures. In all three models, previously used thresholds found in literature resulted in DSC values not significantly different

TABLE IV. Threshold and DSC values for cited and maximum DSC threshold values with threshold intervals within 1σ of DSC_{max} and for all four dogs to have $DSC \geq 0.9$ after adding the temperature uncertainty to the baseline temperature.

Model	Thresholds			
	Cited	DSC_{max}	$DSC_{max} \pm 1\sigma$	$DSC \geq 0.9$
Arrhenius (Ω)	$\Omega = 1.0$	$\Omega = 0.85$	0.10–7.2	0.3–1.7
DSC	0.90 ± 0.03	0.91 ± 0.03		
CEM_{43} (min)	240	950	≥ 210	≥ 540
DSC	0.88 ± 0.05	0.91 ± 0.04		
Threshold temperature (°C)	57	62	59–66	61–62
DSC	0.85 ± 0.06	0.91 ± 0.03		

from peak DSC values. In future studies, we will evaluate treatments with longer exposure times and lower temperatures to determine their effect on the damage predictions. Also, we will compare the different damage models' ability to predict damage due to thermal ablation in brain tumors (rather than normal tissue) to further increase the real-time control and effectiveness of this minimally invasive treatment modality.

ACKNOWLEDGMENTS

[a] Author to whom correspondence should be addressed. Electronic mail: jstafford@mdanderson.org; Telephone: (713) 563-5082; Fax: (713) 563-8842.

[1] H. J. Schwarzmaier, F. Eickmeyer, W. von Tempelhoff, V. U. Fiedler, H. Niehoff, S. D. Ulrich, Q. Yang, and F. Ulrich, "MR-guided laser-induced interstitial thermotherapy of recurrent glioblastoma multiforme: Preliminary results in 16 patients," Eur. J. Radiol. **59**(2), 208–215 (2006).

[2] A. Carpentier, R. J. McNichols, R. J. Stafford, J. Itzcovitz, J. P. Guichard, D. Reizine, S. Delaloge, E. Vicaut, D. Payen, A. Gowda, and B. George, "Real-time magnetic resonance-guided laser thermal therapy for focal metastatic brain tumors," Neurosurgery **63**(1), ONS21–29 (2008).

[3] J. De Poorter, C. De Wagter, Y. De Deene, C. Thomsen, F. Stahlberg, and E. Achten, "Noninvasive MRI thermometry with the proton resonance frequency (PRF) method: In vivo results in human muscle," Magn. Reson. Med. **33**(1), 74–81 (1995).

[4] V. Rieke and K. B. Pauly, "MR thermometry," J. Magn. Reson Imaging **27**(2), 376–390 (2008).

[5] N. McDannold, "Quantitative MRI-based temperature mapping based on the proton resonant frequency shift: Review of validation studies," Int. J. Hyperthermia **21**(6), 533–546 (2005).

[6] M. W. Dewhirst and D. A. Sim, "The utility of thermal dose as a predictor of tumor and normal tissue responses to combined radiation and hyperthermia," Cancer Res. **44**(10), 4772s–4780s (1984).

[7] M. S. Breen, R. S. Lazebnik, M. Fitzmaurice, S. G. Nour, J. S. Lewin, and D. L. Wilson, "Radiofrequency thermal ablation: Correlation of hyperacute MR lesion images with tissue response," J. Magn. Reson Imaging **20**(3), 475–486 (2004).

[8] M. Kangasniemi, C. J. Diederich, R. E. Price, R. J. Stafford, D. F. Schomer, L. E. Olsson, P. D. Tyreus, W. H. Nau, and J. D. Hazle, "Multiplanar MR temperature-sensitive imaging of cerebral thermal treatment using interstitial ultrasound applicators in a canine model," J. Magn. Reson Imaging **16**(5), 522–531 (2002).

[9] R. J. McNichols, A. Gowda, M. Kangasniemi, J. A. Bankson, R. E. Price, and J. D. Hazle, "MR thermometry-based feedback control of laser interstitial thermal therapy at 980 nm," Lasers Surg. Med. **34**(1), 48–55 (2004).

[10] H. J. Schwarzmaier, I. V. Yaroslavsky, A. N. Yaroslavsky, V. Fiedler, F. Ulrich, and T. Kahn, "Treatment planning for MRI-guided laser-induced interstitial thermotherapy of brain tumors—The role of blood perfusion," J. Magn. Reson Imaging **8**(1), 121–127 (1998).

[11] X. He, W. F. Wolkers, J. H. Crowe, D. J. Swanlund, and J. C. Bischof, "In situ thermal denaturation of proteins in dunning AT-1 prostate cancer cells: Implication for hyperthermic cell injury," Ann. Biomed. Eng. **32**(10), 1384–1398 (2004).

[12] X. He and J. C. Bischof, "Quantification of temperature and injury response in thermal therapy and cryosurgery," Crit. Rev. Biomed. Eng. **31**(5–6), 355–422 (2003).

[13] J. C. Bischof and X. He, "Thermal stability of proteins," Ann. N.Y. Acad. Sci. **1066**(1), 12–33 (2006).

[14] J. A. Pearce and S. Thomasen, in *Optical-Thermal Response of Laser-Irradiated Tissue*, edited by A. J. Welch and M. J. C. van Gemert (Plenum, New York, 1995), pp. 561–606.

[15] F. C. Henriques, "Studies of thermal injury, the predictability and the significance of thermally induced rate processes leading to irreversible epidermal injury," Arch. Pathol. **43**(5), 489–502 (1947).

[16] M. Kangasniemi, R. J. McNichols, J. A. Bankson, A. Gowda, R. E. Price, and J. D. Hazle, "Thermal therapy of canine cerebral tumors using a 980 nm diode laser with MR temperature-sensitive imaging feedback," Lasers Surg. Med. **35**(1), 41–50 (2004).

[17] M. D. Sherar, J. A. Moriarty, M. C. Kolios, J. C. Chen, R. D. Peters, L. C. Ang, R. S. Hinks, R. M. Henkelman, M. J. Bronskill, and W. Kucharcyk, "Comparison of thermal damage calculated using magnetic resonance thermometry, with magnetic resonance imaging post-treatment and histology, after interstitial microwave thermal therapy of rabbit brain," Phys. Med. Biol. **45**(12), 3563–3576 (2000).

[18] C. A. Damianou, K. Hynynen, and X. Fan, "Evaluation of accuracy of a theoretical model for predicting the necrosed tissue volume during focused ultrasound surgery," IEEE Trans. Ultrason. Ferroelectr. Freq. Control **42**(2), 182–187 (1995).

[19] P. C. Schulze, T. Kahn, T. Harth, H. J. Schwurzmaier, and R. Schober, "Correlation of neuropathologic findings and phase-based MRI temperature maps in experimental laser-induced interstitial thermotherapy," J. Magn. Reson Imaging **8**(1), 115–120 (1998).

[20] L. Chen, J. P. Wansapura, G. Heit, and K. Butts, "Study of laser ablation in the in vivo rabbit brain with MR thermometry," J. Magn. Reson Imaging **16**(2), 147–152 (2002).

[21] N. Vykhodtseva, V. Sorrentino, F. A. Jolesz, R. T. Bronson, and K. Hynynen, "MRI detection of the thermal effects of focused ultrasound on the brain," Ultrasound Med. Biol. **26**(5), 871–880 (2000).

[22] L. Dice, "Measures of the amount of ecologic association between species," Ecology **26**, 297–302 (1945).

[23] A. P. Zijdenbos, B. M. Dawant, R. A. Margolin, and A. C. Palmer, "Morphometric analysis of white matter lesions in MR images: Method and validation," IEEE Trans. Med. Imaging **13**(4), 716–724 (1994).

[24] K. Van Leemput, F. Maes, D. Vandermeulen, and P. Suetens, "Automated model-based tissue classification of MR images of the brain," IEEE Trans. Med. Imaging **18**(10), 897–908 (1999).

[25] D. W. Shattuck, S. R. Sandor-Leahy, K. A. Schaper, D. A. Rottenberg, and R. M. Leahy, "Magnetic resonance image tissue classification using a partial volume model," Neuroimage **13**(5), 856–876 (2001).

[26] B. Schwabe, T. Kahn, T. Harth, F. Ulrich, and H. J. Schwarzmaier, "Laser-induced thermal lesions in the human brain: Short- and long-term appearance on MRI," J. Comput. Assist. Tomogr. **21**(5), 818–825 (1997).

[27] R. A. Tracz, D. R. Wyman, P. B. Little, R. A. Towner, W. A. Stewart, S. W. Schatz, B. C. Wilson, P. W. Pennock, and E. G. Janzen, "Comparison of magnetic resonance images and the histopathological findings of lesions induced by interstitial laser photocoagulation in the brain," Lasers Surg. Med. **13**(1), 45–54 (1993).

[28] R. J. Stafford, R. E. Price, C. J. Diederich, M. Kangasniemi, L. E. Olsson, and J. D. Hazle, "Interleaved echo-planar imaging for fast multiplanar magnetic resonance temperature imaging of ultrasound thermal ablation therapy," J. Magn. Reson Imaging **20**(4), 706–714 (2004).

[29] J. A. Bankson, R. J. Stafford, and J. D. Hazle, "Partially parallel imaging with phase-sensitive data: Increased temporal resolution for magnetic resonance temperature imaging," Magn. Reson. Med. **53**(3), 658–665 (2005).

[30] R. D. Peters, R. S. Hinks, and R. M. Henkelman, "Ex vivo tissue-type independence in proton-resonance frequency shift MR thermometry," Magn. Reson. Med. **40**(3), 454–459 (1998).

[31] S. A. Sapareto and W. C. Dewey, "Thermal dose determination in cancer therapy," Int. J. Radiat. Oncol., Biol., Phys. **10**(6), 787–800 (1984).

[32] M. W. Dewhirst, B. L. Viglianti, M. Lora-Michiels, M. Hanson, and P. J. Hoopes, "Basic principles of thermal dosimetry and thermal thresholds for tissue damage from hyperthermia," Int. J. Hyperthermia **19**(3), 267–294 (2003).

[33] A. Meshorer, S. D. Prionas, L. F. Fajardo, J. L. Meyer, G. M. Hahn, and A. A. Martinez, "The effects of hyperthermia on normal mesenchymal tissues. Application of a histologic grading system," Arch. Pathol. Lab Med. **107**(6), 328–334 (1983).

[34] N. McDannold, K. Hynynen, D. Wolf, G. Wolf, and F. Jolesz, "MRI evaluation of thermal ablation of tumors with focused ultrasound," J. Magn. Reson Imaging **8**(1), 91–100 (1998).

[35] A. H. Chung, F. A. Jolesz, and K. Hynynen, "Thermal dosimetry of a focused ultrasound beam in vivo by magnetic resonance imaging," Med. Phys. **26**(9), 2017–2026 (1999).

[36]F. A. Jolesz and I. R. Young, "MR-guided thermal ablation of brain tumors," in *Interventional MR: Techniques and Clinical Experience* (Informa Health Care, 1998), p. 123.

[37]K. H. Zou, W. M. Wells III, R. Kikinis, and S. K. Warfield, "Three validation metrics for automated probabilistic image segmentation of brain tumours," Stat. Med. **23**(8), 1259–1282 (2004).

[38]N. McDannold, N. Vykhodtseva, F. A. Jolesz, and K. Hynynen, "MRI investigation of the threshold for thermally induced blood-brain barrier disruption and brain tissue damage in the rabbit brain," Magn. Reson. Med. **51**(5), 913–923 (2004).

[39]R. S. Lazebnik, B. D. Weinberg, M. S. Breen, J. S. Lewin, and D. L. Wilson, "Sub-acute changes in lesion conspicuity and geometry following MR-guided radiofrequency ablation," J. Magn. Reson Imaging **18**(3), 353–359 (2003).

[40]Y. Anzai, R. B. Lufkin, S. Hirschowitz, K. Farahani, and D. J. Castro, "MR imaging-histopathologic correlation of thermal injuries induced with interstitial Nd:YAG laser irradiation in the chronic model," J. Magn. Reson Imaging **2**(6), 671–678 (1992).

[41]M. S. Breen, M. Breen, K. Butts, L. Chen, G. M. Saidel, and D. L. Wilson, "MRI-guided thermal ablation therapy: Model and parameter estimates to predict cell death from MR thermometry images," Ann. Biomed. Eng. **35**(8), 1391–1403 (2007).

[42]J. M. Bland and D. G. Altman, "Statistical methods for assessing agreement between two methods of clinical measurement," Lancet **1**(8476), 307–310 (1986).

[43]R. D. Peters, R. S. Hinks, and R. M. Henkelman, "Heat-source orientation and geometry dependence in proton-resonance frequency shift magnetic resonance thermometry," Magn. Reson. Med. **41**(5), 909–918 (1999).